Doctoral School on Engineering Sciences
Università Politecnica delle Marche

Extended summary

A NUMERICAL AND EXPERIMENTAL ANALYSIS ON NATURAL CONVECTIVE HEAT TRANSFER IN A SQUARE ENCLOSURE WITH PARTIALLY ACTIVE SIDE WALLS

Curriculum: Energetica

Author

Alessia Montucchiari

Tutor(s)

Massimo Paroncini

Date: 30-01-2012

Abstract. An experimental and numerical analysis are performed to investigate the effect on the size, number and positions on natural convection in square enclosures (H=0.05m) filled with air with partially active side walls. the thermal sources are applied on the vertical side of the enclosure; test involve two different configuration. The first configuration included three cases: Case 1 the hot strip in the middle of one wall, and the cold strip at the middle Case 2 in the top or Case 3 at the middle of the opposite wall. In the second configuration there are four sources and for Case 4 a heat source pair is located on the left lateral wall, while the other pair is located on the right wall, for Case 5 the heat strips are alternately located on the sidewalls. For each configuration measures are performed with different temperatures of the hot strip. The fluid flow, heat transfer, and heat transport characteristics were illustrated by averaged Nusselt number, isotherms, streamlines, obtained with Holographic interferometry, Particle Image Velocimetry and Fluent 12.1.4..Only for the first configuration, a 2D particle image velocimetry (PIV) was utilized to measure the velocity fields at the same Rayleigh numbers. In particular we analysed the distribution of the velocity vectors and their modulus inside the cavity. For the Case 1, 4, 5 each

measured quantity was compared with the numerical value and its distribution, obtained with the finite volume code Fluent 12.1.4. From the analysis developed has been observed that as the number of sources and reducing the size of the heat exchange increases.
Results show that the heat transfer increase with an increase on the number of the thermal sources; Case 4 produces the fastest dynamic field and the highest Nusselt number

Keywords. Holographic interferometry, Natural convection, Numerical simulation, Nusselt number, Particle Image Velocimetry.

1 Introduction

Natural convection in enclosures plays a major role in a number of applications: cooling of electronic or mechanical systems, solar energy, insulating materials, building design, etc. In most cases knowledge about natural convection is used either to maximize or minimize the heat exchanged in a particular situation. For this reason, many authors have given particular attention to this kind of phenomenon and different studies have been done, especially in the recent years, both numerically and experimentally. In such cases, the size and the location of the heater and cooler play an important role in the fluid flow and in the heat transfer mechanism.

Poulikakos [1] and Ishihara et al. [2] studied enclosures with partially heated and cooled zones on a single sidewall. Chu, Churchil et al [3] studied the effect of heater size, location, aspect ratio and boundary condition on two dimensional laminar natural convection in rectangular channels. Ntibarufata et al. [4] numerically investigated natural convection in partitioned enclosures with localized heating from below. Aydin et al. [4] studied numerically the convection of air in a rectangular enclosure with a localized heating from below and the symmetrical cooling from the sides. Ho and Chang [4] investigated natural convection heat transfer in a vertical rectangular enclosure with two-dimensional discrete heating. November et al. [5] studied rectangular enclosures heated from below and cooled along one side

The effect of the size and the location of the heat and cool strips play an important role in the fluid flow and in the heat transfer mechanism for square cavity.

Torkoglu et Yucel [6] investigated the effects of the heater and cooler location on natural convection in square cavities.

Nithyadevi et al [7] worked on natural convection heat transfer in the cavities with partially active sides for different aspect ratios. November et al. [8] studied rectangular enclosures heated from below and cooled along one side. Ganzarolli et al. [9] investigated the case of a cavity symmetrically cooled from the sides, Valencia and Frederich [10] reporting numerical analysis of natural convection of air in a square cavity with partially active side walls for five different heating locations.

Randriazanamparany et al. [11] present a numerical study of unsteady natural convection inside an air-filled square cavity, heated from two opposite sides and cooled from the other two sides.

In this work, an experimental and numerical analysis is performed to explore the heat transfer characteristics for natural convection in a square enclosure.

This study is focused on the effects of the size the position and the number of sources in the enclosure.

The holographic interferometry is used to study thermal behavior of the heat transfer while 2D PIV is used to define the velocity field. The objective of the heat transfer analysis is the investigation of the Nusselt numbers distribution at different Rayleigh numbers.

For each configuration studied, the experimental and numerical correlation connecting the Rayleigh numbers with the corresponding Nusselt numbers are analyzed.

The isothermal patterns obtained with the holographic interferometer are compared with the ones obtained from a numerical study performed using Fluent 12.1.4 with a two dimensional model.

Finally, for each configuration, a relationship between the average Nusselt numbers and the correspondent Rayleigh numbers is elaborated.

2 Experimental equipement

2.1 Holographic interferometry

The holographic interferometer (Fig. 1) is used to determine the temperature distribution inside the cell. The main elements of the holographic interferometry system are: a test cell, filled with air at atmospheric pressure (Pr= 0.71); a thermal system (two thermostatic baths, the thermal circuit and the temperature control system); a pneumatic auto-leveling table; a laser light source; all the necessary optical instrumentation. The test cell is an enclosure having a square section (side H= 0.05 m) and a "deepness" of 0.42 m (Fig. 2); this length is considered big enough to neglect the end effects and to employ a two-dimensional model. All the surfaces of the enclosure are made of 0.05 m thick Plexiglas (PMMA); this material has proven a good compromise between workability, transparency to laser radiation (in the case of PIV) and thermal insulation properties for realizing the cell's walls. The end vertical walls, in the case of the holographic interferometry cell, are made up of glass to enable the passage of the laser beam.

Figure 1. Holographic interferometer

Figure 2. Test cavity

The natural convective heat transfer was studied for two differences configuration ζ =H/2 ζ =H/4 and H height values of the thermal sources.

In the first configuration three cases are investigated:

Case 1 there are two identical active sources (hot and cold) on the vertical walls symmetrical position (case middle-middle, M-M).

Case 2 the hot source is located in the middle of the left lateral wall while the cold sources is placed on the top of the wall (case middle- top, M-T)

Case 3 the hot source is maintained in the middle of the wall while the cold sources is placed on the bottom of the wall (case middle-bottom, M-B)

In the second configuration two cases are investigated:

Case 4 a heat source pair is located on the left lateral wall, while the other pair is located on the right wall

Case 5 the heat strips are alternately located on the sidewalls

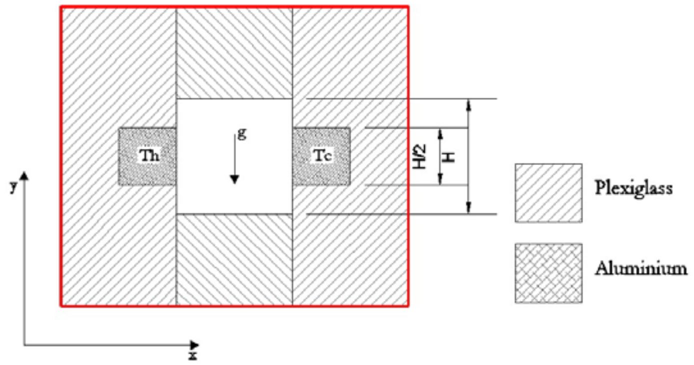

Figure 3. Case 1M-M

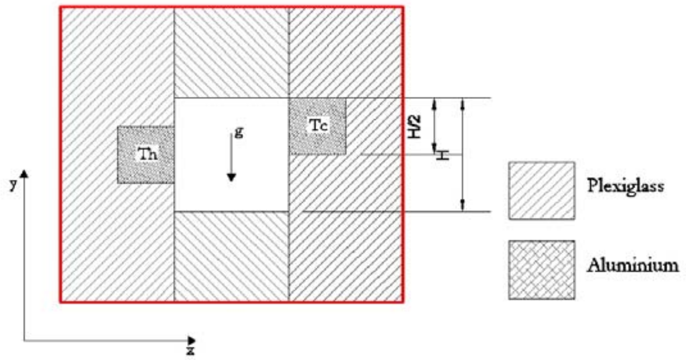

Figure 4.Case 2 M-T

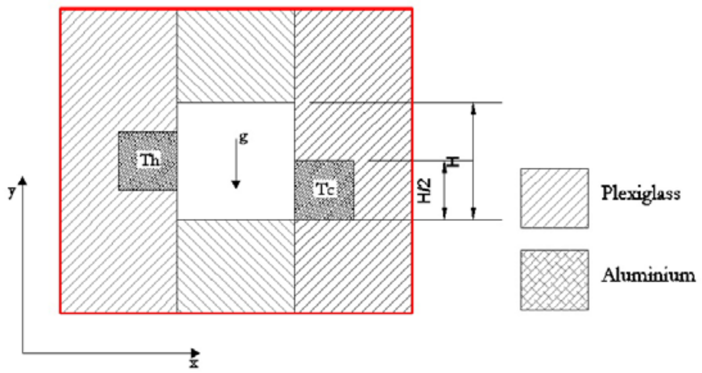

Figure 5.Case 3 M-B

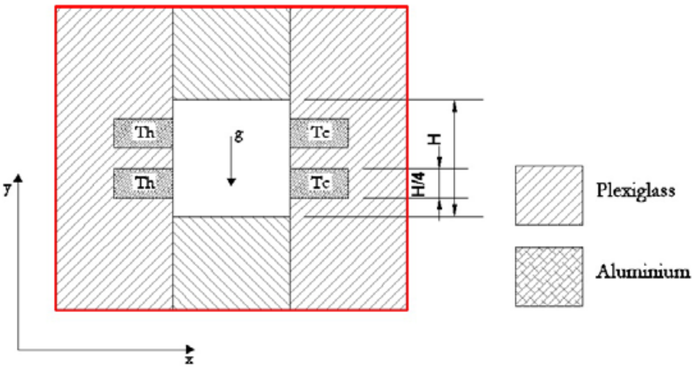

Figure 6.Case 4

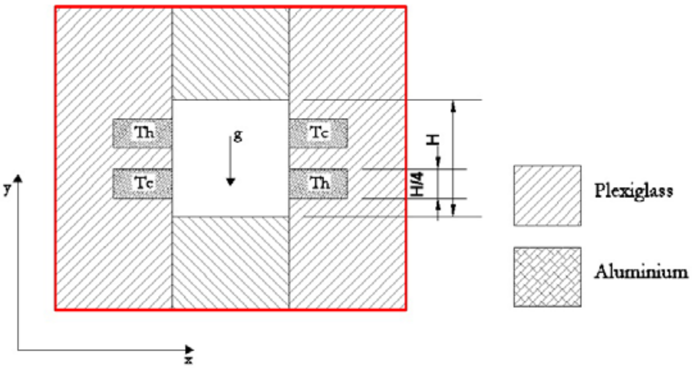

Figure 7.Case 5

The hot and cold strips are made of aluminium and have a dimension l = H/2 = 0.025 m; they extend for the entire test cell deepness (0.42 m). For the first configuration, the hot strip is in the middle of the left wall while the cold strip is moved in three different positions in the right wall, creating three different cases (see Fig. 3, 4, 5). For the first configuration the hot sources first are located on the left wall while cold strip are in the sidewall then the strip arealternately located

For each configuration, the hot strip is heated and maintained at a temperature Th using a thermostatic bath. This temperature is changed from one test to another to obtain different Rayleigh numbers. The cold strip on the right wall is kept at a temperature Tc by another thermostatic bath, set at 291.15 K and it is constant during all experiments.

The rest of the thermal circuit is the two thermostatic baths with their respective connecting pipes. The thermostatic baths are model “Proline e RP 1840”, manufactured by “Lauda Corporation”; the baths accuracy is 0.01 °C and the volume of each bath is 18 l.

Each pipe connecting the thermostatic baths with the inlet and outlet valves of the two sidewalls, is coated by a neoprene skin (about 0.02 m thick) for thermal insulation. The thermal fluid is a mixture of 75% water and 25% glycol (percentages in volume at 295.15 K). The temperature measuring system is made up of seven copperconstantan thermocouples connected with an ice point reference made by “Kaye”, model “K170” and an “Hp Agilent 34970A” acquisition system. Six of them are used to measure the temperature on the strips, three on the hot strip and three on the cold strip, located 1 mm under the surface of the test volume (little circles in Fig. 2). These temperatures cannot be used as a reference for the temperature distribution of the fringes during the interpretation of the interferograms (because of the diffraction effects and the high fringes density close to the strips). For this reason the last thermocouple is positioned in the middle of the air region in order to give a reference temperature for analyzing the interferograms. The difference between the three temperature values recorded on the aluminum strips is about 0.2 K and therefore it is possible to consider strips as isothermal. The Ra number of each experiment is calculated considering the average temperature between those recorded on each strip.

The laser used is model “532-50 DPSS”, manufactured by “Coherent” laser, a diode-pumped solid state frequency-doubled Nd:YAG laser that emits an output beam at a 532 nm wavelength (green).

The optical set-up allows the use of either double-exposure or real time holographic interferometry techniques for the steadystate and temporal evolution measurements of the heat transfer process. The real-time technique is also used to check the presence of plume oscillations. The real time interferograms are obtained through a fringe finite field, while a fringe infinite field is used in the double exposure interferograms; in this way the fringe pattern is comparable to the distribution of the isothermal lines.

Uncertainties of this kind of measures are difficult to be defined, but for a small number of fringes (less than 30), according to Hauf and Grigull [12] the expected accuracy can be about 10%.

2.2 PIV

The 2D PIV system employed for the measures is composed of several apparatus for different functions (Fig. 8):
- a measuring cavity;
- a thermal system (two thermostatic baths, the thermal circuit and the temperature control system);.
- an oil nebulizer device;
- a laser;
- a CCD camera;
- a control and acquisition system.

Figure 8.2D PIV experimental apparatus

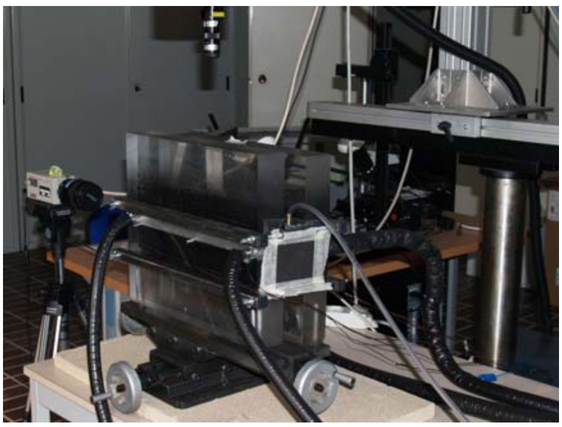

Figure 9.Test cavity

The cavity (Fig. 9) is similar to the one used for holographic interferometry; differences are:
- the PIV cavity has only one side closed by a glass window; the other extremity of the cavity is closed by a thermally insulating low reflecting surface, since there is no need for optical access of the cavity from both sides;
- in the PIV system, all inside surfaces are painted with a low reflecting color; only the upper wall is not painted, since it is crossed by the 532 nm wavelength laser radiation.

The thermal circuit is identical to the one of the holographic interferometry, and so is the temperature control system, except for the fact that the seventh thermocouple is used for checking the room temperature in the PIV laboratory; this temperature and also the relative humidity value in the measuring room can be changed by a heating/cooling system.

During tests room temperature is set at 295.15 K and relative humidity is kept at 50%. The seeding used is sunflower oil; it is nebulized by a compressed air device, creating particles of diameter about 1 mm, and it is sprinkled inside the cavity by a hole positioned in its rear end. A relaxation time of 20 s from the sprinkle has proven long enough for the flux to stabilize and the image acquisition to start.

A double head Nd:YAG laser is employed for producing the luminous plane; the laser shade has a wavelength of a 532 nm. The laser employed for measures is a “Solo II” model, manufactured by “New Wave Research”; it is operated with double Q-switch trigger.

In this way it is possible to produce a double laser pulse; the main adjustable variables concerning laser firing are the “time between pulses” and the “double pulse frequency”. “Time between pulses” influences the path of the particles between the first and the second image recorded, and has to be adjusted with the mean velocity in the field. During our campaign the time between pulses was in the range 6500÷10,000 μs (smaller time intervals for faster fields). “Double pulse frequency” is the inverse of the time between the double pulses sequences (always kept equal to 6.1 Hz). Since in the present case, streamlines and flowmaps are an average of a fixed number of couples of images, this variable also has an important influence. With a 6.1 Hz frequency, the time for recording 100 couples of images (that is the number usually employed in our measuring campaign) is about 16.5 s. During this time particles sprayed in the cavity may stabilize in some undesired way, creating blank spots or stripes; if possible, also this time has to be kept small.

The image capturing device is a CCD camera (model “C8484- 05C” manufactured by “Hammatsu”). The 60 mm lens is covered by a filter (wavelength l¼ 532 nm) in order to record only direct or scattered light from the laser source. Images resolution is 1344·1024 pixels; the effective measured field is about 1000·1000 pixels.

The laser and the camera are controlled by a pc; the software and part of this control hardware are by “Dantec Dynamics” [13]. The signal processing is based on the cross-correlation technique, and is applied by the software used through a Fast Fourier Transform; the interrogation areas for the PIV technique are size 32·32 pixels, a 50% overlap of the areas is used both in the horizontal and vertical directions, and also a moving-average validation methods is used in order to accept or reject vectors from the crosscorrelation-process; the validation method used is based on the assumption that the velocity field is continuous, and rejects vectors via a comparison with their neighbors: a vector is an outlier, and therefore it is rejected, if it differs too much in intensity from its neighbors. Rejected vectors are then substituted by the average of the surrounding vectors. Signal to noise maps of the field are used to validate a database, and only if the map shows a good signal the acquisition is accepted.

In the case of PIV, it is impossible to perform an analytical analysis of errors; anyways it is possible to say that the difference in maximum velocities both for different recordings during the same test than for different recordings on different tests is generally ±1.0%; if average velocity is considered this error increases to ±1.5%. This gives an idea of how big random errors are, but, of course, doesn't define systematic errors that could effect the-measure.

3 Numerical analysis

The Fluent solution methods are almost standard and a particular description of the mathematical model can be found in the Fluent User's Guide. The simulation is developed by a finite volume code Fluent 12.1.4 using the boussinesq approximation for air and is performed with a 2d approximation.

3.1 Segregated solver

The numerical results are carried out through the segregated solvers for $1\ 10^4 < Ra < 1\ 10^5$, and they are compared with the experimental data. In this study, a second order upwind implicit scheme is employed in the conservation equations as it happens for the spatial discretization; the pressure interpolation is provided by the Body Force Weighted scheme; the pressure velocity coupling is provided by the SIMPLE algorithm, and a two-dimensional model is used with the condition of laminar flow. The diffusion terms are central-differenced with a second order accuracy.

3.2 Numerical setting

The test cell is reproduced with real dimensions. The temperatures of the heated strips are assigned in order to obtain the analyzed Rayleigh numbers as in the experimental analysis. The top and the bottom surfaces are thought to consider the conductive heat flux through the plexiglass walls. The plexiglass element is introduced too in the Fluent model. It is necessary to simulate the conductive heat transfer between these elements using the conjugate heat transfer. A uniform mesh structure with a square cell is performed. A study of the mesh was carried out preliminarily to obtain the lowest number of cells necessary to perform an analysis with results that are independent from the choice of the cell number. Appreciable changes have not been observed in the results that are obtained through a mesh of over 22,500 cells. For example, for $Ra = 10^5$, the increase of the mesh size from $150 \cdot 150$ to $200 \cdot 200$ produces a change in the average Nusselt of about 0.81%. This change in the results touched a maximum value of 1.04% in the local Nusselt number calculated on the hot strip for both configuration. Under these conditions, the variables used to compare the numerical results and the experimental ones showed an independent behavior with respect to the grid size and any particular dynamic structure can be solved.

3.3 Simulation procedure

The calculation starts with the steady. The numerical average Nusselt numbers (Nuave) on the heating elements are given by:

$$\overline{Nu} = \frac{q_{tot} / A_h}{k \cdot \Delta T / H} \tag{1}$$

where qtot= the heat transfer rate directly computed by Fluent; Ah = the heater surface that is considered and k = the thermal conductivity of the air evaluated at the heating strips temperature.

The local Nusselt numbers (Nuh) are also referred to the heat sources, and they are calculated as:

$$Nu_h = \frac{q''}{k \cdot \Delta T / H} \tag{2}$$

where q"=the heat flux computed by Fluent on each cell of the mesh.

4 Results and discussion

4.1 Interferometry holographic

It is investigated the effect of heat sources using the holographic interferometry both with the real time technique and the double exposure technique.

The real-time interferograms are obtained with a finite-fringe field, while a infinite-fringe field is used in the double exposure interferograms; so doing the fringe pattern shows directly the distribution of the isothermal lines.

The experimental Rayleigh numbers investigated through the holographic interferometry vary from about $1.18 \cdot 10^4$ to $2.30 \cdot 10^5$.
The Rayleigh numbers are defined as:

$$Ra = \frac{(g \cdot \beta(T_h - T_c) \cdot H^3}{\nu \cdot a} \tag{3}$$

The dimensionless parameters used are:

$$X = \frac{x}{H}; Y = \frac{y}{H}; \theta = \frac{(T - T_c)}{(T_h - T_c)}; \varepsilon = \frac{l}{H} \tag{4}$$

The local Nusselt number – Nu(Y) – on the hot sources is calculated thanks to the expression:

$$Nu_h(Y) = -\left.\frac{\partial \theta}{\partial X}\right|_{X=0} \tag{5}$$

The average Nusselt number – Nuave – on the heat sources is given by the relationship:

$$Nu_{ave} = \frac{1}{\varepsilon}\int_{0}^{\varepsilon} Nu_h(Y)dY \tag{6}$$

For ζ = H/4 configuration the Nu_{higher} and Nu_{lower} are calculated. All experimental Nu values are reported in Table 2. For each configuration the expression of Nu(Ra) is defined; it is in the form:

$$Nu_{cal} = aRa^b \tag{7}$$

The values of the parameters of eq. (7) are shown in Table 4. Also the correlation coefficient R^2 of each function is reported. R^2 is an indicator that describes the fitting of the function to the experimental data, and is defined as follows:

$$R^2 = 1 - \frac{SSE}{SST} \tag{8}$$

Where

$$SST = \sum_{J=1}^{n}\left[k_j - \frac{1}{n}\sum_{j=1}^{n}k_j\right]^2 \tag{9}$$

And

$$SSE = \sum_{J=1}^{n}\left(k_j - h_j\right) \tag{9}$$

Where kjs= the n experimental values and hjs are the corresponding calculated values.

The closer R^2 is to 1, the better the relationship fits the experimental data. Plots of the experimental points and of the calculated functions are reported in Figure 10, 11.

Differences between experimental and calculated Nu numbers are always less than 4.5%. In particular the worst result (4.38%) is recorded for the MT configuration for Ra= $1.7\cdot10^5$. For the lowest Ra numbers in all configurations, Nusselt numbers are much smaller than the others. In the MB configuration for Ra > $1\cdot10^5$, the average Nusselt numbers are smaller than those of the other configurations. This aspect is connected to the flow field development and will be further investigated in the PIV analysis.

Table 1. Experimental Nusselt number for the Caso 1 (M-M)

Ra	Nu exp	Nu exp	Δ (%)
6.19E + 04	3.00	3.05	1.65
1.21E + 05	4.61	4.42	4.14
1.77E + 05	5.27	5.45	3.50
2.28E + 05	6.29	6.27	0.24

Table 2. Experimental Nusselt number for the Caso 2 (M-T)

Ra	Nu exp	Nu exp	Δ (%)

5.54E + 04	3.36	3.37	0.40
1.18E + 05	4.79	4.74	1.12
1.73E + 05	5.54	5.62	1.50
2.25E + 05	6.35	6.33	0.36

Table 3. Experimental Nusselt number for the Caso 3 (M-B)

Ra	Nu exp	Nu exp	Δ (%)
5.85E + 04	2.63	2.66	-1.00
1.18E + 05	4.10	3.95	3.80
1.74E + 05	4.98	4.89	-0.40
2.25E + 05	5.61	5.65	-0.70

Table 4. Parameters Nu corr

Cases	a	b	R^2
1 M-M	0.0054	0.5659	0.9950
2 M-T	0.0068	0.5534	0.9892
3 M-B	0.0251	0.4487	0.9983

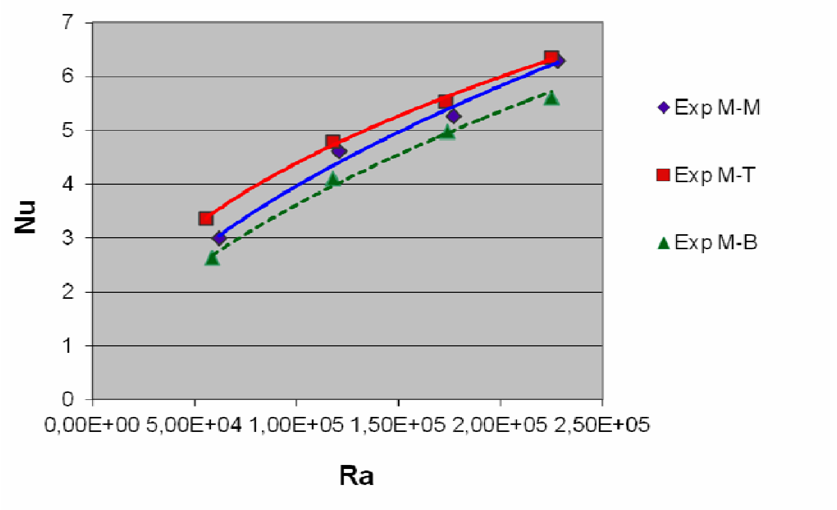

Figure 10. Expemerimental average Nusselt number Case 1, 2, 3

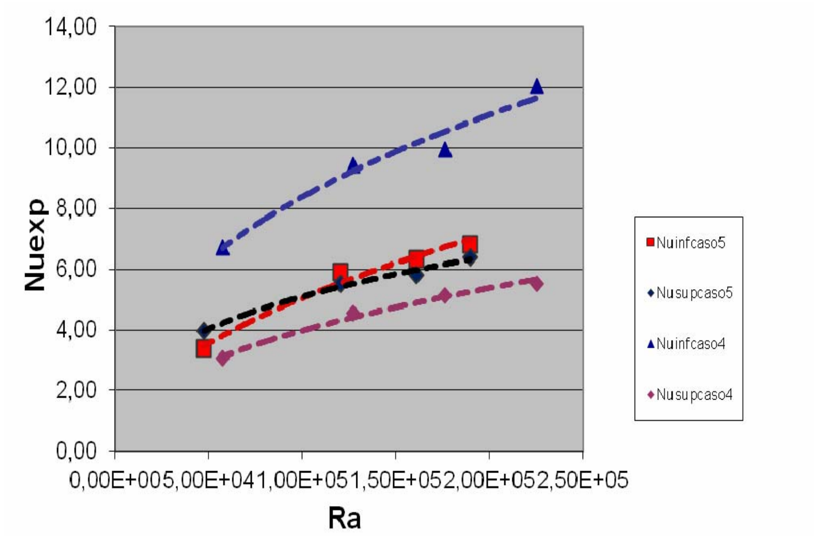

Figure 11. Expemerimental average Nusselt number Case 4, 5

Table 6. Experimental and calculated Nusselt numbers for case 4

Case 4							
Higher sources				Lower sources			
Ra	Nu	Nucal	Δ(%)	Ra	Nu	Nucal	Δ(%)
5.73E+04	3.07	3.12	-1.62	5.73E+05	6.71	6.70	0.14
1.27 E+05	4.56	4.42	3.07	1.27E+05	9.43	9.24	2.01
1.78 E+05	5.14	5.09	0.97	1.78E+05	9.96	10.54	-5.82
2.30 E+05	5.52	5.67	-2.71	2.30E+05	12.06	11.65	3.39

Table 7. Experimental and calculated Nusselt numbers for case 5

Case 5							
Higher sources				Lower sources			
Ra	Nu	Nucal	Δ(%)	Ra	Nu	Nucal	Δ(%)
4.75E+04	3.96	3.97	0.17	4.75E+04	3.40	3.47	2.13
1.20 E+05	5.52	5.42	-1.84	1.20E+05	5.90	5.57	-5.99
1.61 E+05	5.82	5.98	2.62	1.61E+05	6.33	6.45	1.88
1.90 E+05	6.40	6.32	-1.34	1.90E+05	6.80	7.01	3.01

Table 8. Experimental correlation parameters.

	Case 1	Case 4		Case 5	
		Higher sources	Lower sources	Higher sources	Lower sources
	Nu_{exp}	Nu_{exp}	Nu_{exp}	Nu_{exp}	Nu_{exp}
a	0.0068	0.0261	0.08030	0.1063	0.0147
b	0.5534	0.4366	0.4038	0.3361	0.5075
R^2	0.9892	0.9898	0.9728	0.9907	0.983

The heat transfer rate for each source across the whole cavity is described by the average Nusselt number.

The invariance of the fringes to Ra about 10^4 indicated the conduction as the major heat exchange mechanism inside this range of Ra.

In Figure 13, the fewer fringes indicate the presence of a weak convection while for Ra > 10^4 a well-developed convective motion is clear.

In Figure. 13, it is possible to see four examples of double exposure interferograms at different Rayleigh numbers. The fringes (Fig. 13) are comparable qualitatively to the isothermal lines (Fig. 14): each line is characterized by a different temperature level. It is possible to note a comparison with the distribution of the isothermal lines obtained for both configurations. The average Nusselt numbers on the heat sources at various Rayleigh numbers are presented in Table 1, 2, 3, 7, 8. The contribution of natural convection increases with the Rayleigh numbers.

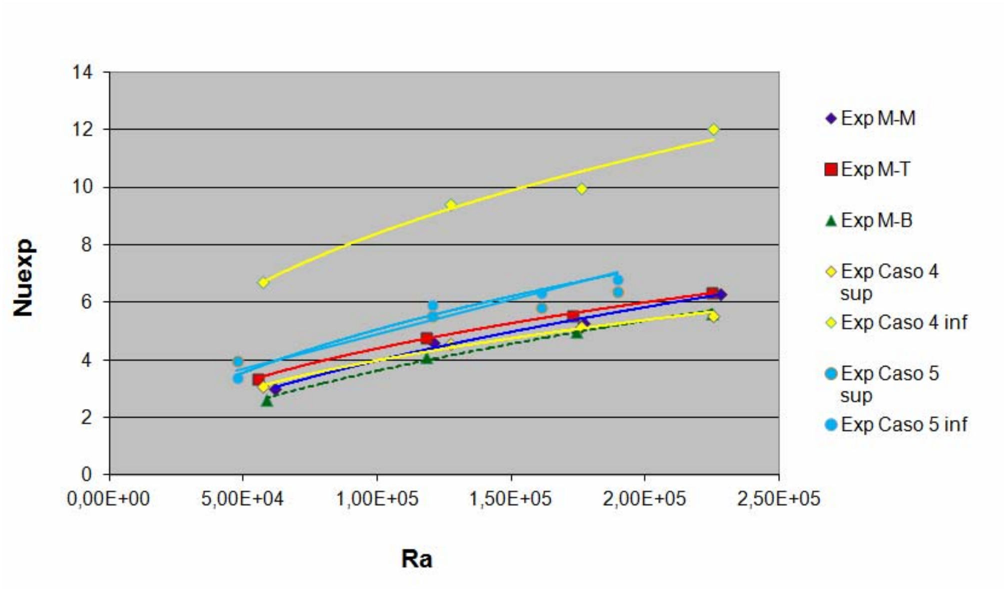

Figure 12. Expemerimental average Nusselt number Case 4, 5

It is possible to observe as the growing of the Rayleigh numbers creates a progressive development of the natural convective heat transfer indicated through the growing of the Nusselt numbers.

Analyzing the interferograms for both configurations for Ra = $6.19 \cdot 10^4$ and for Ra = $5.73 \cdot 10^4$, it is possible to see that there are not many isotherms near the surface of the left wall; while in the other images, a lot of fringes are located near the left side of the cavity. It happens because at low Rayleigh numbers, the natural convection development is different. It is possible to observe that for both configurations, the fringes are located in the bottom of the enclosure. In particularly in the high part of ζ = H/4 configuration, there is a stratification of the flux more evident than in the other configuration. For Ra = $6.19 \cdot 10^4$ and for Ra = $5.73 \cdot 10^4$, the conduction heat transfer mode becomes dominant over the convection. Analyzing the average Nusselt numbers of Table 1, 2, 3, 7, 8 it is possible to note that for Ra = 10^4, the average Nusselt numbers are very small compared to the others. This aspect indicates a reduced heat transfer as underlined through the lack of fringes near the hot surfaces in the first interferograms.

Then, it is possible to note that the fringes in the high and down portion of the cavity are not perpendicular to the surface, showing that the top and the bottom of the enclosure is not perfectly adiabatic.

Only for Ra > 10^5 the convection can be observed; the phenomenon is characterized by a change in the isothermal curves near the heat sources. For both configurations studying in depth the image of Figure 13 between Ra = $1.00 \cdot 10^5$ and Ra = $2.5 \cdot 10^5$, this aspect changes and it is possible to note that the conduction heat transfer mode is relegated in the

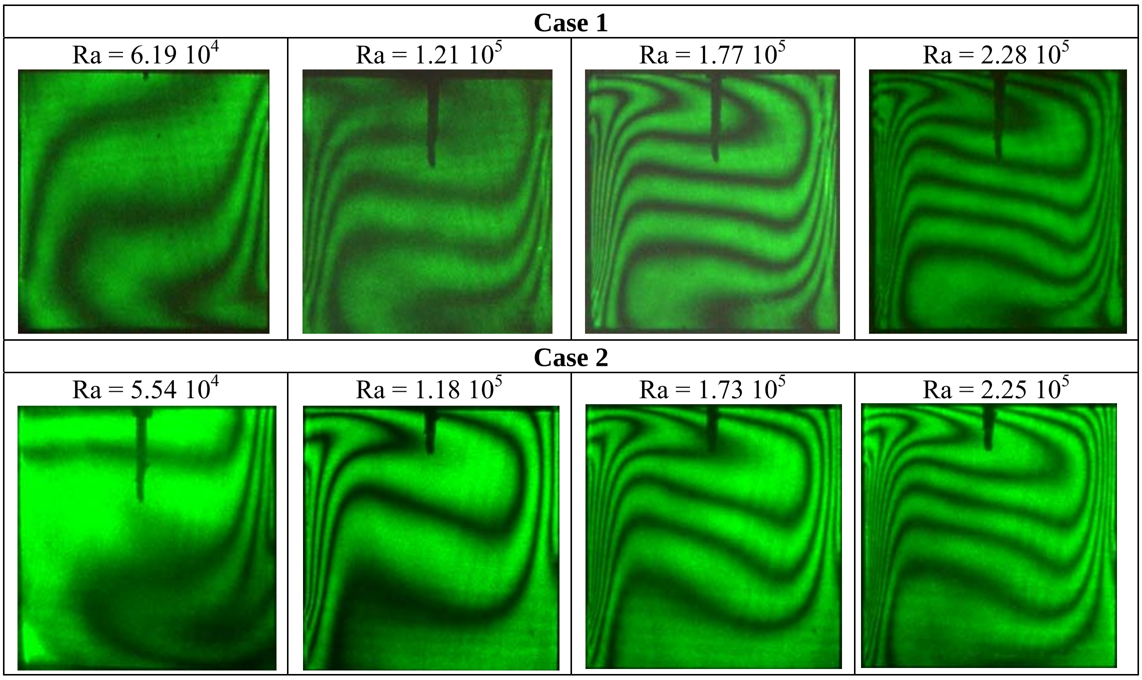

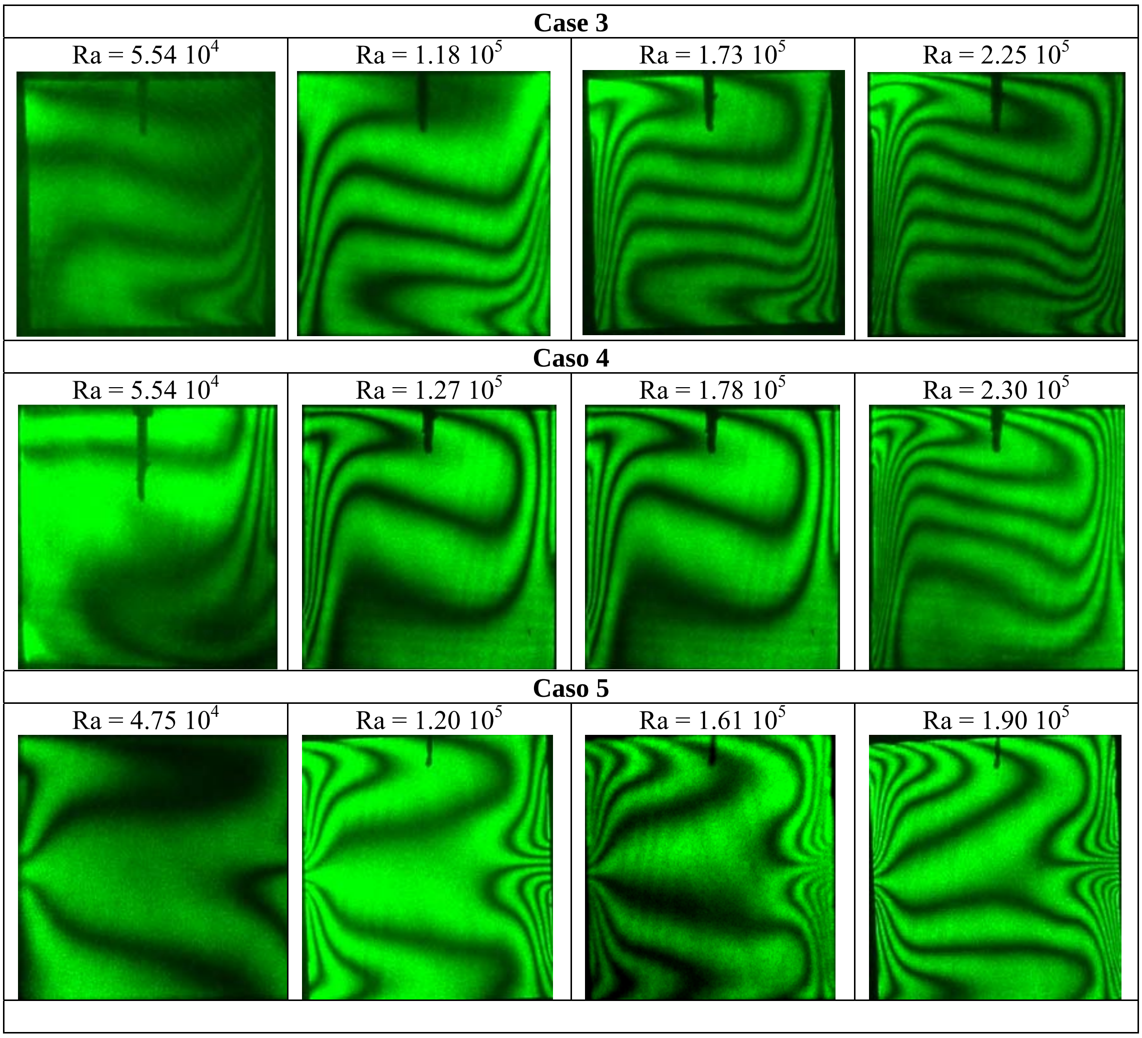

Figure 13. Interferograms from double exposition for case 1, 2, 3,4,5

upper and down of the enclosure; there are more fringes near the left side of the enclosure: this aspect shows greater thermal gradient and thus the Nusselt number increases and, in the trend of the Nusselt numbers, the heat transfer increases.

In both configurations for Ra about 10^5, a modification occurred in the isothermal experimental fields. In fact owing to the increase in buoyancy, motion intensity increases, which implies that the heated fluid comes close to the cooled wall thus bringing to larger temperature gradients at the wall as also proved by the increased deformation of the isotherms near the cold strips.

In ζ = H/2 and ζ = H/4 configuration, there is the important reduction in the efficiency of the heat transfer between the lateral surfaces and the centre zone. In fact analyzing Figure 10, it is possible to find few fringes on the internal zone of the cavity where the temperature gradient is lower than the one near the hot strips.

4.2 PIV

Streamlines are lines always tangent the particle's path. The analysis of the streamlines plots gives important indications about the characteristics of the velocity field in terms of direction of the velocity vectors. Streamlines are particularly useful for analyzing the characteristics of the flow, and especially position and dimension of the vortexes in the enclosure.

Streamline plots are shown in Figure. 14. A comment on the streamlines plots follows; in the first part observations are developed by confronting plots describing the same configuration. In the second part, different configurations are compared.

In the MB configuration only one vortex is present in the field, even for the highest Ra analyzed. For the lowest Ra, it is positioned almost in the middle of the cavity, and it changes in shape and position with the increase of Δ T; the center of the vortex moves to the high left corner, and the shape flattens on the horizontal direction. Even if there is no birth of a second vortex, the right edge of the vortex tends to fall down as an effect of the increasing influence of the cold surface. In the MM configuration there is only one measure with a single vortex; for Ra = 10^5 the second vortex already appears and the streamlines plot is almost symmetrical. With the increase of Ra the symmetry vanishes, since the highest vortex flattens in a similar way as in the previous configuration. In the MT configuration the low Ra streamlines are similar to those of the MB configuration, but mirrored on the xy bisector. The increase of Ra produces the formation of the second vortex (Ra=1.78 105). Keeping on increasing the Ra, the highest vortex tends to flatten as in the previous configurations, but in a weaker way. The low vortex, instead, is much bigger than in the previous cases.

The comparison between streamlines of similar Ra, but different configurations allows the following observations:

- in all cases the difference between the MB streamlines and the other configurations' streamlines are more evident than those between the streamlines of the MM and MT configurations, mainly due to the presence of only one vortex in the MB plots;

- the trend seems to show an increase of the dimension of the low vortex and a change in the shape of the high vortex as the cold source is moved up along the wall;

-between the lowest Ra numbers and the highest ones, there is a Ra range where differences between the MM and the MT configurations are smaller than in all other cases and streamlines plots tend to be quite similar (Ra = $1.5\cdot10^5 \div 2.5\cdot10^5$). In Table 5 the maximum and average velocity values of each field are reported; these values give general indications about the entire field; the maximum and average velocity values are in accordance with the Nu values obtained by Holographic Interferometry; also in Figure 16 and 17 the experimental average and maximum values and the linear regression obtained for each configuration are showed; also contour maps of the velocity are in Figure. 15. As in the case of the Nu numbers, velocity (both average and maximum ones) are in the order MB<MM< MT, although, as the Ra increases, MM tends to approach MT values.

In the velocity maps the intensity of each velocity vector is represented by a grade of the grey scale: light colors correspond to low speeds, while dark colors correspond to high speeds. All images have the same scale, with 20 different grey degrees going from 0ms□ 1 to a maximum velocity value corresponding to 0.075 ms□ 1. In all configurations, at low

Ra, the field shows a simple circular clockwise moving velocity map; small velocities are in the middle of the field and in the corners; higher velocities are next to the strips; some other areas with a big velocity are next to the ceiling on the left side, and next to the floor, on the right side. Also in all cases, as the Ra increases, the fast areas expand and the slow center contracts and looses symmetry: a faster edge develops that "eats" the slow field from the left side, and only a small slow tip remains on the top that is positioned in the center of the highest vortex. As the Ra increases, the slow tip becomes more and more thin, and the bottom of the high vortex increases in speed. The fast velocity fields next to the walls become faster, meaning that there is a high velocity gradient in those areas. In the MT configurations, the presence of the second vortex can be identified by a fast field internal to the central slow one in its bottom edge: this area represents the top of the low vortex and expands with the increase of Ra.

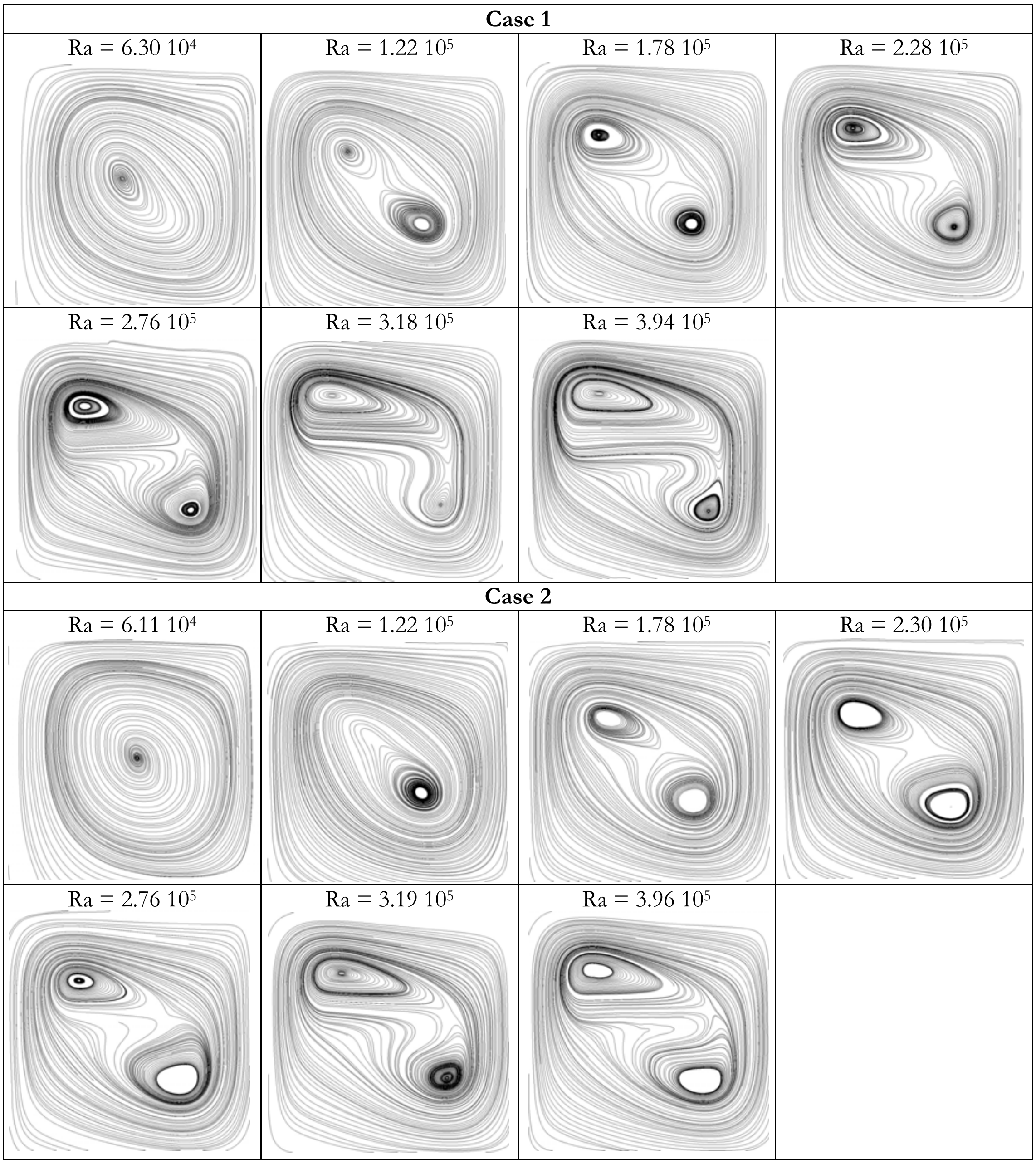

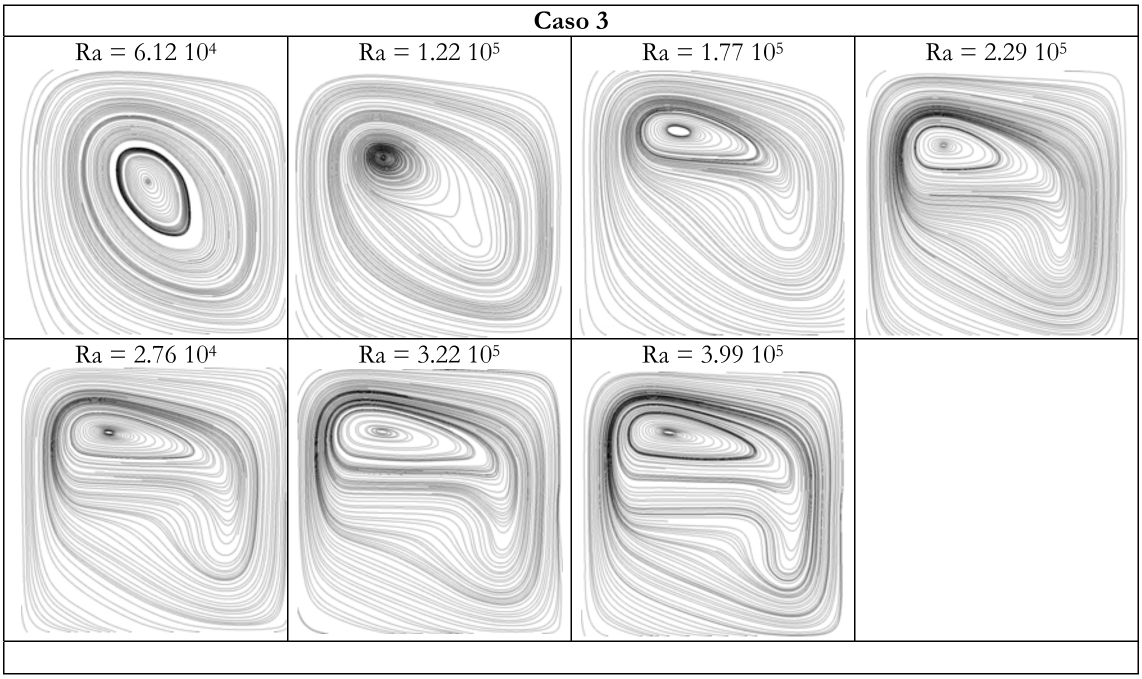

Figure 14. Streamlines from PIV for case 4, 5.

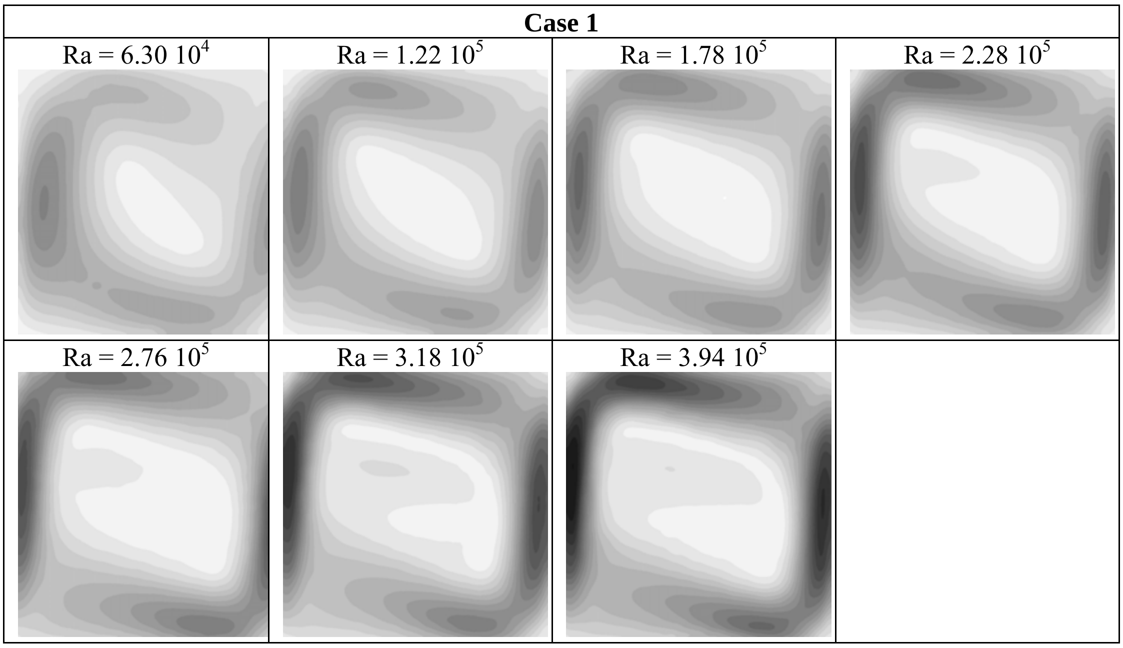

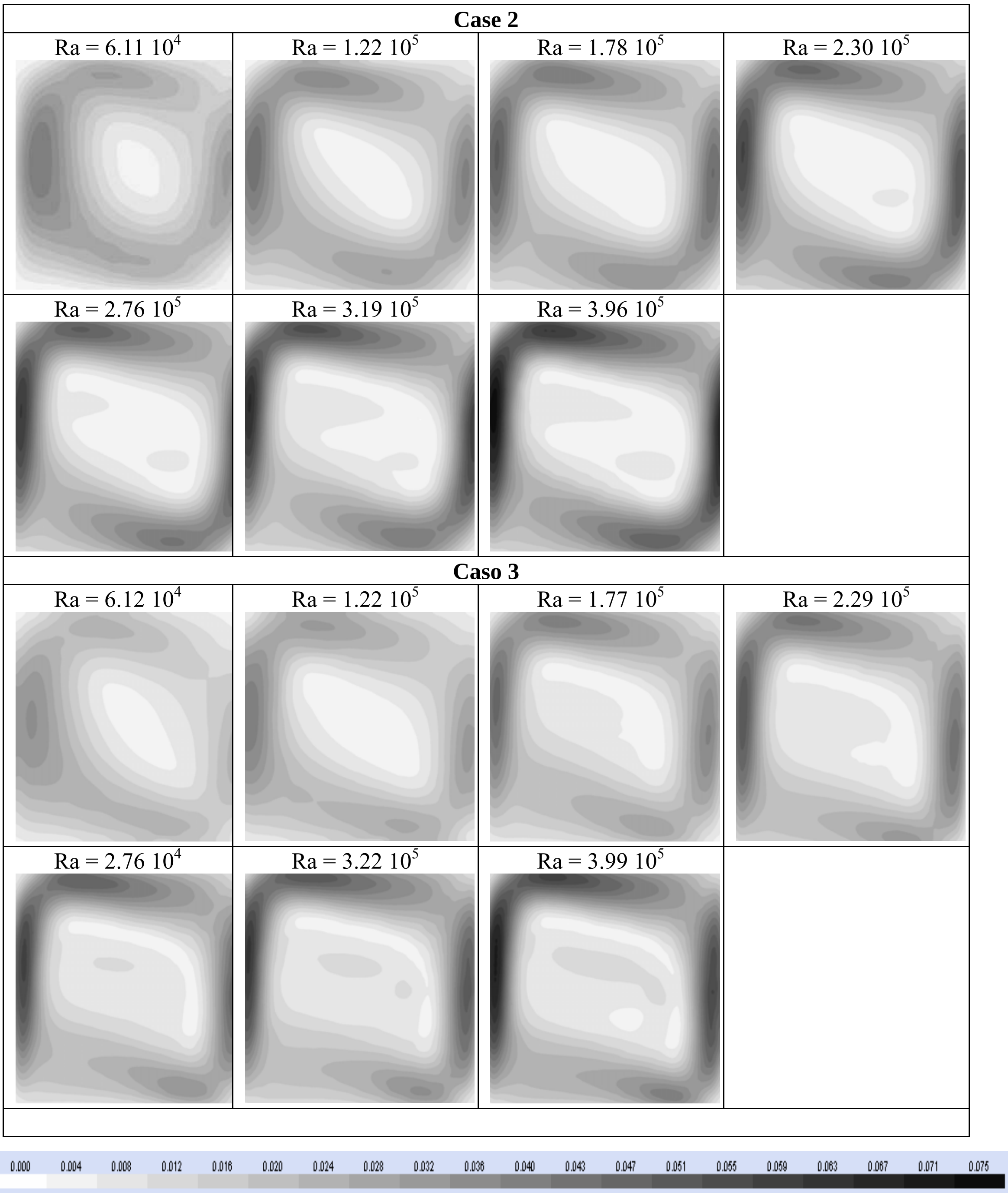

Figure 15. Velocity map from PIV for case 4, 5.

Table 9. Experimental average and maximum velocity values [m s□ 1].

Config 1	Ra	Vave	Vmax
Caso 1	$6.12 \cdot 10^4$	0.014	0.032
Caso 1	$1.22 \cdot 10^5$	0.015	0.038

Caso 1	$1.77 \cdot 10^5$	0.016	0.045
Caso 1	$2.29 \cdot 10^5$	0.018	0.050
Caso 1	$2.76 \cdot 10^5$	0.019	0.057
Caso 1	$3.22 \cdot 10^5$	0.020	0.060
Caso 1	$3.99 \cdot 10^5$	0.022	0.067
Caso 2	$6.30 \cdot 10^4$	0.015	0.036
Caso 2	$1.22 \cdot 10^5$	0.016	0.039
Caso 2	$1.78 \cdot 10^5$	0.017	0.045
Caso 2	$2.28 \cdot 10^5$	0.019	0.054
Caso 2	$2.76 \cdot 10^5$	0.020	0.057
Caso 2	$3.18 \cdot 10^5$	0.021	0.062
Caso 2	$3.94 \cdot 10^5$	0.023	0.071
Caso 3	$6.11 \cdot 10^4$	0.016	0.039
Caso 3	$1.22 \cdot 10^5$	0.018	0.042
Caso 3	$1.78 \cdot 10^5$	0.019	0.048
Caso 3	$2.30 \cdot 10^5$	0.021	0.055
Caso 3	$2.76 \cdot 10^5$	0.021	0.059
Caso 3	$3.19 \cdot 10^5$	0.021	0.064
Caso 3	$3.59 \cdot 10^5$	0.023	0.068
Caso 3	$3.96 \cdot 10^5$	0.024	0.073

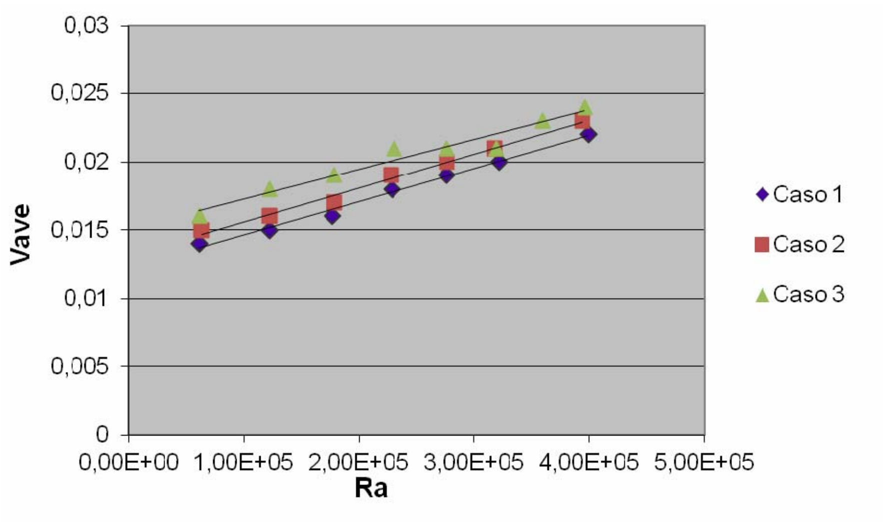

Figure 16. Average velocity [m s^{-1}] at different Ra numbers; experimental points and tendency lines (least squares method).

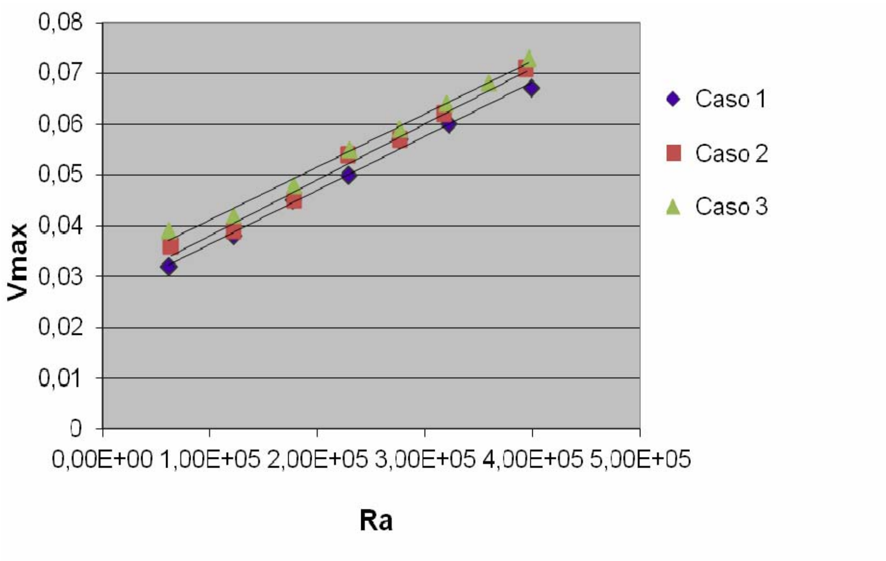

Figure 17. Maximum velocity [m s^{-1}] against Ra; experimental points and tendency lines (least squares method)

4.3 Numerical results

The experimental analyses are compared with the numerical simulations (Fig. 18). It is already possible to see a good qualitative agreement between the numerical and the experimental temperature distribution in the enclosure. In fact, it is possible to note that the behavior of the numerical isothermal lines is the same as the others obtained through the experimental study.

In the numerical stream functions, Figure 19, it is possible to note the existence of two recirculation zones for ζ = H/2 configuration and one recirculation zone for ζ = H/4 configuration. This assumption change depending on the Rayleigh numbers and the position of the sources.

For Case 4, the heat picked up by the fluid from the top source on the left sidewall is not conveyed to the strip on the bottom but the one on the top of the right sidewall. On the other hand, the heat from the bottom source is conveyed by the fluid not only to the strip on the top but also the one on the bottom of the opposite sidewall. So their buoyancies are thus composed together which creates only one recirculation zone in the cavity. In fact the fluid is driven upward by the strips in the left side wall and then downward by the strips on the right wall. The heat picked up by the fluid from the top strip on the left wall is not conveyed to the strip on the bottom but the one on the top of the right wall.

However, at the top of the cavity, the temperature gradient in the fluid is simply lower in this region due to the effects of the thermal stratification.

For Case 1 configuration at the highest Rayleigh number, it is possible to note two vortexes but their size changes with the increase of the Rayleigh number.

For Case 4 configuration for Ra = $1.78 \cdot 10^5$, it is possible to note a vortex at the top right corner of the cavity that depends on the motion of air due to the heating of the sources; this heat transfer moves the air toward the top of the cavity, and so it is cooled by the lateral walls so the fluid is pushed down. For Ra = $2.30 \cdot 10^5$, there is a horizontal development of the recirculation zone. This flow field feature can generate an important influence on heat transfer.

Analyzing the images for Ra = $6.19 \cdot 10^4$ and for Ra = $5.73 \cdot 10^4$, it is possible to see a monocellular motion. The strength of the buoyancy effect is not enough strong to create two separate recirculation zones, and consequently, the Nusselt numbers are low.

For Case 1 configuration for Ra > 10^5, the air motion can generate two different structures: thanks to the streamlines (Fig. 18) and the velocity maps (Fig. 20); it is possible to notice that the velocity fields grow up with the Rayleigh numbers.

For case 4 the heat picked up by the fluid from the top source on the left sidewall is not conveyed to the strip on the bottom but the one on the top of the right sidewall. On the other hand, the heat from the bottom source is conveyed by the fluid not only to the strip on the top but also the one on the bottom of the opposite sidewall. So their buoyancies are thus composed together which creates only one recirculation zone in the cavity. In fact the fluid is driven upward by the strips in the left side wall and then downward by the strips on the right wall. The hot bottom strip on the upper creates a forced convection, however, at the top of the cavity at the top of the cavity the temperature gradient in the fluid is simply lower in this region due to the effects of the thermal stratification.

For case 2 the buoyancies are decomposed into two groups that generates two recirculation zones with an elliptical shape, one in the upper region and the other in the lower region as shown by streamlines Figures 18. The numerical stream functions show that the hot upper strip channels the flow to opposite strip though a recirculation zone, the hot bottom strip generates a heat flow that influences both the bottom strip on the opposite sidewall as indicated by the averaged Nusselt number (Tab. 12).

Analysing the streamlines and velocity maps, it is possible to notice for both cases the velocity fields grow up with the Rayleigh numbers. For case 1 for Ra ≥ 10^5 the strength of the buoyancy effect is not enough strong to create two separate recirculation zones and consequently the Nusselt numbers are low, while for case 4 for Ra > 10^5 the air motion can generate two different structures and the natural heat transfer grows up (Tab. 6, 7). In Tables 1, 6, 7, 10, 11, 12 it is possible to note that the heat transfer is developed more in the source below than in the top one, as indicated by the Nusselt numbers.

It is possible to determinate a curve to interpolate numerical numbers for the cases 1, 4, 5 analyzed (Fig. 21 and 22), show the average normalized Nusselt numbers on the heat sources at different Rayleigh numbers.

Calculated Nusselt numbers are shown in Tables 10-12 for cases 1, 4, 5. A relationship between the average Nusselt numbers and the correspondent Rayleigh numbers is also elaborated for three casee of the numerical studies. The correlation coefficients R^2 of each function are reported inTables 13. When the sources are split into smaller segments (from case 1 to case 5), the number of sources increases, and therefore the heat transfer increases.

When the sources are located alternately on the walls (from case 4 to case 5), the heat transfer decreases as confirmed by total Nusselt numbers (Tables 11 and 12).

Combining above size and position effects of the sources together, it is possible to notice that heat transfer is consistently enhanced (1 → 5 → 4).

This means that the heat transfer in enclosures due to discrete sources could be enhanced when the source splits the discrete elements into more smaller segments.

Case 1

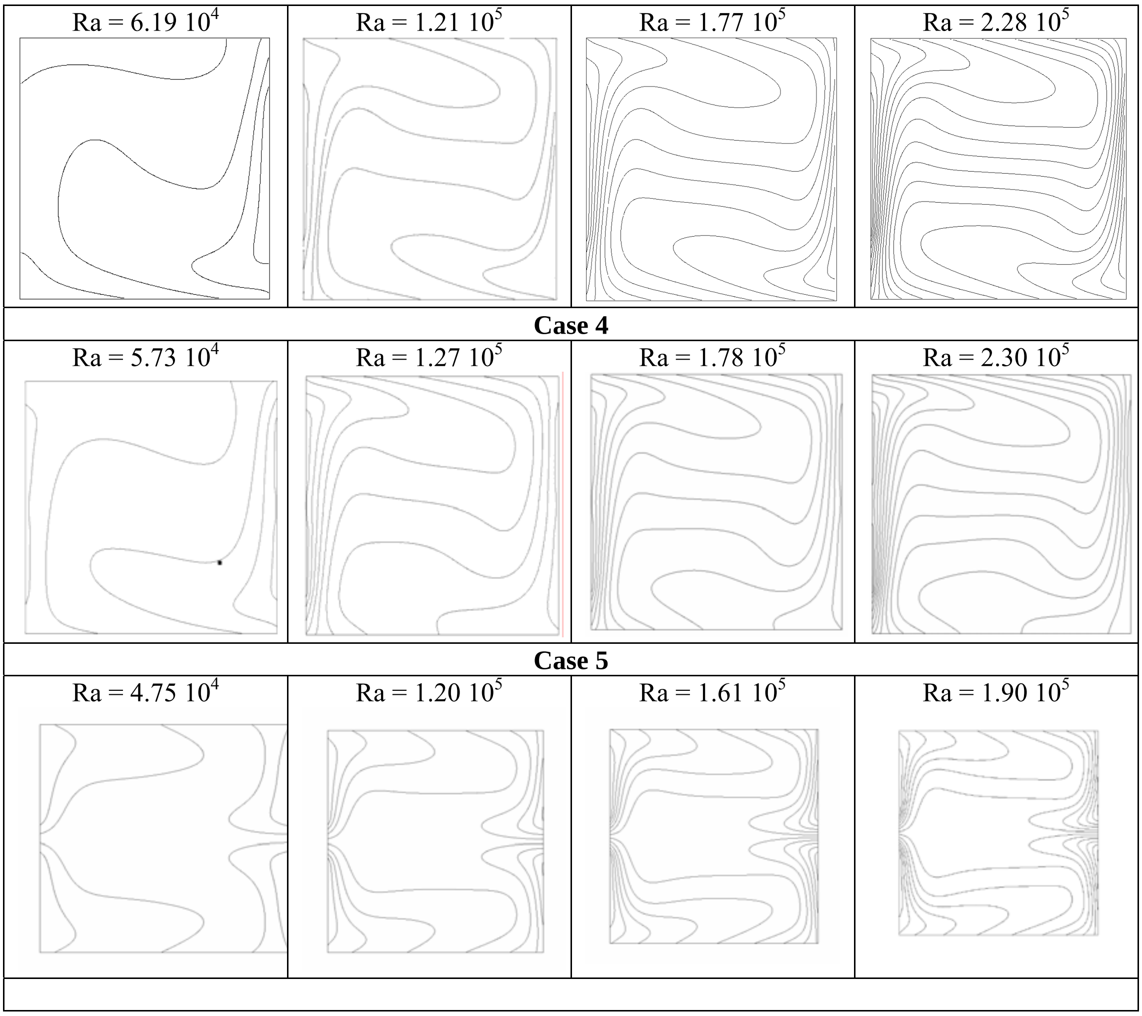

Figure 18. Numerical isothermal lines for case 1, 4, 5.

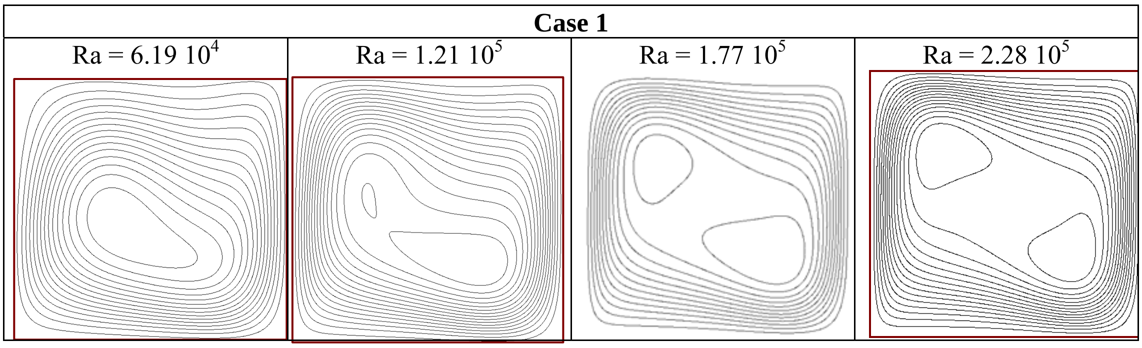

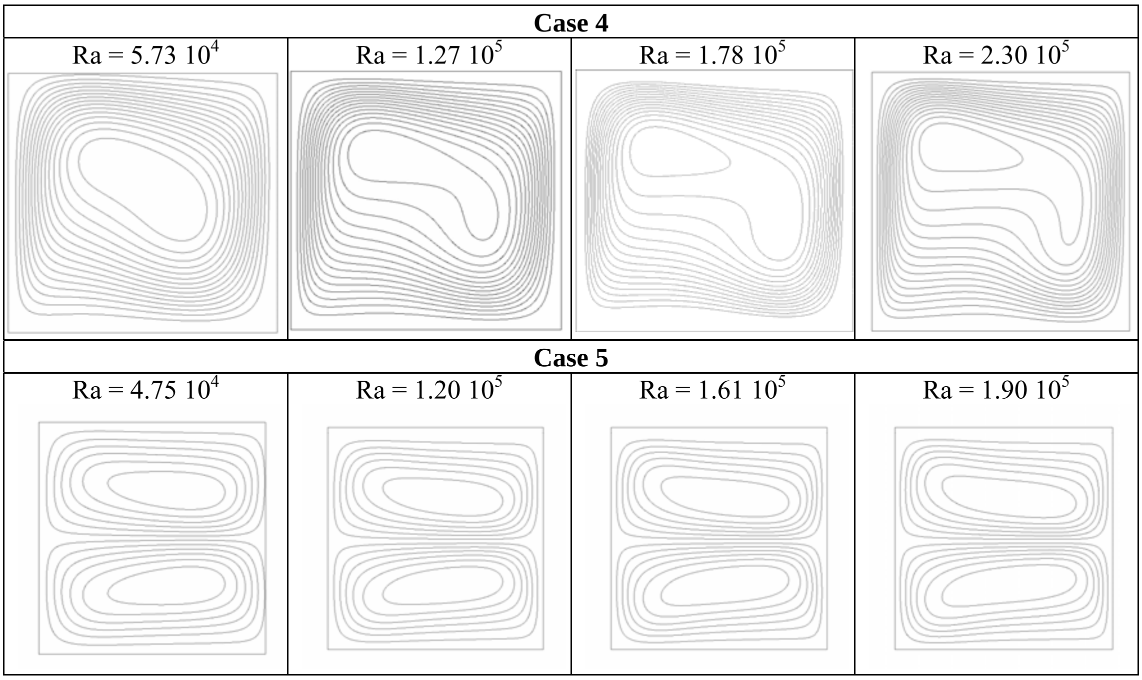

Figure 19. Numerical streamlines for case 1, 4, 5.

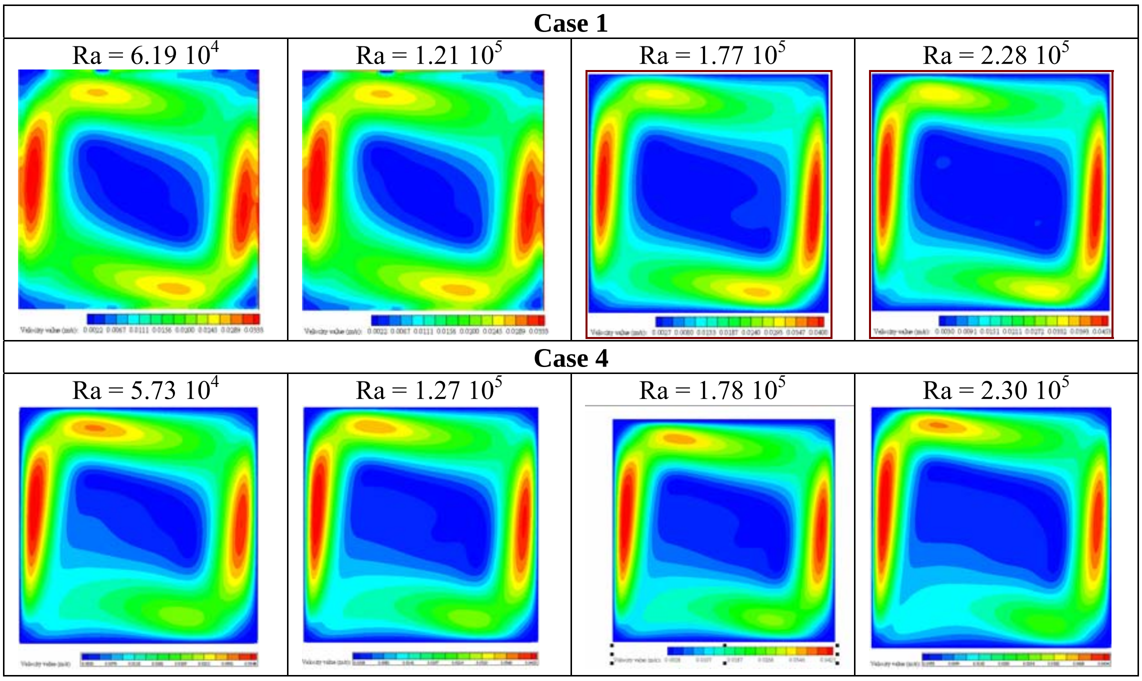

Case 5			
Ra = 4.75 10^4	Ra = 1.20 10^5	Ra = 1.61 10^5	Ra = 1.90 10^5

Figure 20. Numerical velocity maps for case 1, 4, 5

Table 10. Numerical and calculated Nusselt numbers

Case 1			
Ra	Nu	Nucal	Δ(%)
6.19E+04	3.24	3.27	-0.92
1.21E+05	4.52	4.48	0.88
1.77E+05	5.47	5.51	-0.73
2.28E+05	6.20	6.25	-0.80

Table 11. Numerical and calculated Nusselt numbers

Case 4							
Higher sources				Lower sources			
Ra	Nu	Nu-cal	Δ(%)	Ra	Nu	Nu-cal	Δ(%)
5.73E+04	3.67	3.36	-1.10	5.73E+04	6.96	6.86	-1.40
1.27 E+05	4.41	4.47	1.34	1.27 E+05	8.25	8.40	1.76
1.78 E+05	4.71	4.88	3.48	1.78 E+05	8.82	9.15	3.57
2.30 E+05	5.41	5.22	-3.64	2.30 E+05	10.15	9.76	-4.01

Table 12. Numerical and calculated Nusselt numbers

Case 5							
Higher sources				Lower sources			
Ra	Nu	Nucal	Δ(%)	Ra	Nu	Nucal	Δ(%)
4.75E+04	4.35	4.29	-1.42	4.75E+04	4.25	4.18	-1.61
1.20 E+05	5.35	5.56	3.84	1.20 E+05	5.37	5.63	4.54
1.61 E+05	6.01	6.01	0.41	1.61 E+05	6.14	6.17	0.51
1.90 E+05	6.52	6.51	-3.19	1.90 E+05	6.74	6.50	-3.65

Table 13. Numerical correlation parameters.

	Case 1	Case 4		Case 5	
		Higher sources	Lower sources	Higher sources	Lower sources
	Nu_{exp}	Nu_{exp}	Nu_{exp}	Nu_{exp}	Nu_{exp}
a	0.0113	0.2063	0.4289	0.2106	0.1349
b	0.5108	0.2617	0.2531	0.28	0.3189
R^2	0.999	0.9632	0.9542	0.9705	0.9691

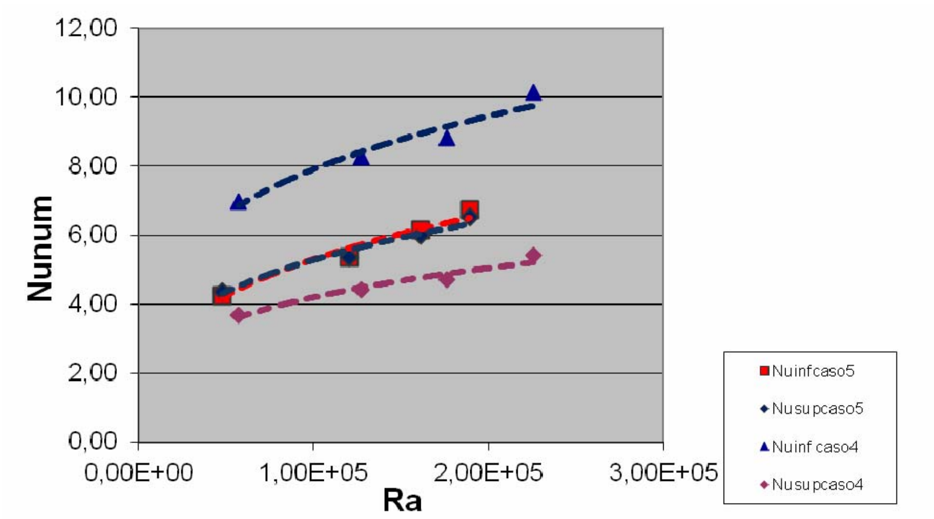

Figure 21. Numerical Nusselt number for Case 4, 5

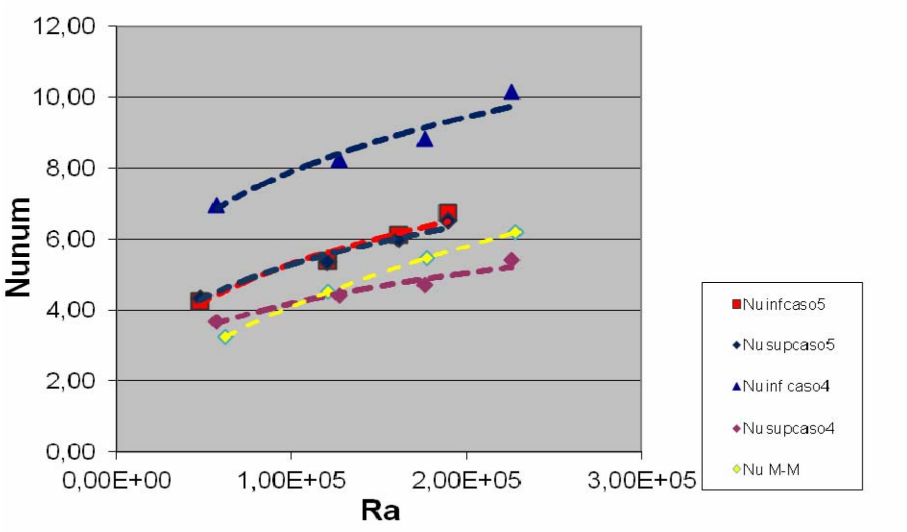

Figure 22. Numerical Nusselt number for Case 1, 4, 5

For all cases analyzed, the differences between the experimental and calculated Nusselt numbers are less than -5.99 %. In particular the worst result (-5.99 %) is recorded for the case 3 for Ra = $1.20 \cdot 10^5$.

While the differences between the numerical and calculated Nusselt numbers are less than 3.96 % for case 2 for Ra = $1.83 \cdot 10^5$.

5 Conclusion

The effects of the different sizes and positions of the heat sources on the natural convective heat transfer in a square cavity is experimental and numerically investigated.

This study is carried out experimentally and numerically mode through the holographic interferometry, PIV and through the finite volume code Fluent 12.1.4. Streamlines plots, velocity maps, temperature fields and Nu numbers are shown; also Nu(Ra) relations are drawn for each configuration. A comparison between the experimental data and numerical ones present a good agreement for the Rayleigh number range from 10^4 to 10^5.

For all cases analyzed, Nusselt numbers and the velocity values increase according to the Rayleigh numbers. This proves a better development of the natural convective heat transfer with the increase of the Rayleigh numbers. The size and the position of the heat sources influence the velocity field.

Analysing the experimental and numerical results the variation of total heat transfer rate change by two regimes: conduction for Ra = 10^4 and convection for Ra = 10^5.

For the first configuration a particular phenomenon is found: while Nu(Ra) plots have similar slopes in the M-B and M-T cases, the Nu(Ra) for the M-M case is more steep, so that it almost reaches the M.T plot for Ra=2.5 10^5. This trend suggests that for Ra numbers higher than about Ra=3.0 10^5 the M-M configuration becomes the most efficient one.

When the strips are split into smaller segments (from ζ =H/2 to ζ =H/4), the number of sources increases and therefore the heat transfer increases.When the arrangement changes from case 1 to case 4 the number of recirculation zones decreases in the cavity and the heat transfer increases for $10^4 <$ Ra $< 10^5$, while when the arrangement changes from case 4 to case 5 the number of recirculation zones increases in the cavity and the heat transfer decreases. This means that the heat transfer in enclosures due to discrete sources could be enhanced when the source splits the discrete elements into more smaller segments.

The location of the hot sources influences the velocity field. In particular, analysing the velocity maps, it is possible to notice that the velocity fields of the case 4 are faster than the other ones. This fact, that is confirmed by total Nusselt numbers calculated through the holographic interferometry, proves a better development of the natural convective heat transfer in the case 4.

References

[1] P. Poulikakos, *Natural convection in a confined fluid-filled space driven by a single vertical wall with warm and cold regions*, ASME J. Heat Transfer, Vol. 107 , 1985, pp.867–876.

[2] Ishihara, R. Matsumoto, A. Senoo, *Natural convection in a vertical rectangular enclosure with localizing heating and cooling zones*, Heat Mass Transfer, Vol. 36, 2000, pp. 467–472.

[3] H.S.S. Chu, S.W. Churchill, S.V. Patterson, *The effect of heater size, location, aspect ratio and boundary conditions on two-dimensional, laminar, natural convection in rectangular channels*, ASME J. Heat Transfer, Vol. 98, 1976, pp.194-201.

[4] E. Ntibarufata, M. Hasnaoui, E. Bilgen,P. Vasseur, *Natural convention in partitioned enclosures with localized heating*, Int. Journal of Heat and Mass Transfer, Vol. 42, 1999, pp. 2345-2355.

[5] Aydin, O. and Yang, W-J, *Natural convection in enclosures with localized heating from below and symmetrical cooling from sides*, Int. J. Num. Methods Heat Fluid Flow, Vol. 10, 2000, pp. 519-529.

[6] H. Tűrkoglu, N. Yűcel, *Effects of heater and cooler location on natural convection in square cavities Numerical Heat Transfer*, Vol. 27, 1995, pp. 351-358.

[7] N. Nithyadevi, P. Kandaswamy, J. Lee, *Natural convection in a rectangular cavity with partially active side walls*, Int. J. Heat Mass Transfer, Vol. 50, 2007, pp. 4688-4697.

[8] M.November, M. W. Nansteel, *Natural convection in rectangular enclosures heated from below and cooled along one side*, Int. Journal of Heat and Mass Transfer, Vol. 30 , No.11, 1987, pp. 2433-2440.

[9] M. M. Ganzarolli, L. F. Milanez, *Natural convection in rectangular enclosures heated below and symmetrical cooled from the sides*, Int. Journal of Heat and Mass Transfer, Vol. 38 , No.6, 1995, pp. 1063-1073.

[10] A. Valencia, R. L. Frederick, *Heat transfer in square cavities with partially active vertical walls,* Int. J. Heat Mass Trans., Vol.32, No.8, 1989, pp. 1567-1574.

[11] M. Randriazanamparany, A. Skouta, M. Daguenet, *Numerical study of the transition toward chaos of two-dimensional natural convection within a square cavity,* Numerical Heat Transfer, Vol. 48, 2005 pp.127–147.

[12] W. Hauf, U. Grigull, Optical Methods in Heat Transfer, in: J.P. Harnett, T.F. Irvine, Jr(Eds.), Advances in Heat Transfer, Academic Press, New York, 1970, pp. 133–311.

[13] *"FLUENT User's Guide",* Fluent Incorporated

[14] Dynamics Studio Software Introduction to PIV Dantec Dinamics GmbH, 2000, Publication number: 9040U3625.